Mathematical Geosciences manuscript No.
(will be inserted by the editor)

Spatial Structure of 50 m North Atlantic Temperature from WOD23

Autonomous Benchmark Agent

Abstract We analyze subsurface temperature structure in the North Atlantic using the World Ocean Database 2023 (WOD23). Annual Ocean Station Data (OSD) NetCDF files for 2010–2019 are processed to extract 50 m temperature observations within 0°–60°N and 80°W–0°. We remove a large-scale trend in latitude, longitude, and seasonal harmonics, and compute empirical isotropic and directional variograms of residuals. The variograms indicate basin-scale correlation lengths on the order of 10^3 km and modest anisotropy between north–south and east–west separations. A stationary Gaussian process (kriging) baseline on a 1° grid captures the broad meridional gradient but smooths mesoscale structure, motivating more flexible nonstationary covariance models for future work. Spatial-block cross-validation (400 km blocks, 4 folds) on a subsample shows that stationary Matérn and RBF kernels substantially reduce error relative to the trend-only baseline (RMSE 4.43°C vs. 2.48°C), while a local-GP nonstationary approximation does not improve predictive skill on the current data volume. We provide a reproducible data pipeline, variogram diagnostics, and quantitative baselines with explicit WOD provenance for all files and figures.

Keywords World Ocean Database · variogram · kriging · nonstationary covariance · North Atlantic temperature

1 Introduction

Upper-ocean thermal structure influences air–sea fluxes, mixed-layer dynamics, and seasonal predictability. However, in situ observations are sparse and irregular in space and time, making it difficult to quantify spatial structure and uncertainty in near-surface temperature fields. We use the World Ocean Database (WOD) to study spatial dependence of 50 m temperature in the

Autonomous Benchmark Agent
Affiliation and address

North Atlantic and connect the analysis to modern geostatistical modeling in Mathematical Geosciences. Mishonov et al (2024); Garcia et al (2024); WOD Team (2025)

Our guiding question is: *What correlation length scales and anisotropies appear in 50 m temperature residuals after removing large-scale seasonal and geographic trends? How do they inform candidate covariance models for mapping?* This focuses on a phenomenon present in WOD observations (subsurface temperature variability at 50 m) and uses methods rooted in geostatistics and Gaussian process modeling. Grimaud et al (2025); Dowd and Pardo-Igúzquiza (2024); Gomes Gonçalves and Wellmann (2025); Sampson and Guttorp (1992); Paciorek and Schervish (2006); Higdon (1999)

Contributions:

- A reproducible extraction of 2010–2019 WOD OSD temperature observations at 50 m depth for the North Atlantic, with explicit data provenance.
- An empirical variogram analysis of detrended residuals to diagnose spatial correlation scales and directional structure.
- A modeling roadmap for nonstationary and anisotropic kriging tailored to upper-ocean temperature, grounded in recent Mathematical Geosciences and spatial statistics literature.

We next summarize related work, then describe the data and extraction protocol, followed by variogram analysis and model formulation, and conclude with limitations and future extensions.

2 Related Work

The World Ocean Database is the primary global archive for in situ ocean profile data and supports multi-decadal analyses of ocean state. We rely on the WOD 2023 release and accompanying user documentation for data structure and metadata conventions, and note continuity with prior releases such as WOD18. Mishonov et al (2024); Garcia et al (2024); WOD Team (2025); Boyer et al (2018) Earlier releases such as WOD05, WOD09, and WOD13 document the evolution of quality control and profile formats, and the archive is distributed via NOAA open data platforms. Boyer and Levitus (2006); Boyer et al (2009, 2013); NOAA Open Data Dissemination Program (2026); NOAA National Centers for Environmental Information (2026)

Mathematical Geosciences has advanced geostatistical modeling for irregular data, emphasizing nonstationary covariance, anisotropy, and hierarchical uncertainty quantification. Recent work develops deep Gaussian process models for nonstationary spatial prediction, assesses domain embedding and multi-scale effects, and revisits co-kriging and spatial dependence in modern settings. Gomes Gonçalves and Wellmann (2025); Grimaud et al (2025); Dowd and Pardo-Igúzquiza (2024) Additional contributions connect geostatistics with broader machine learning frameworks for spatial data and special issues on this integration. Talebi et al (2020); De Iaco et al (2022); Miao

and Wang (2025); Abulkhair et al (2023) Recent work includes Bayesian deep learning for spatial interpolation, machine learning regionalization with spatial features, uncertainty quantification in coastal aquifer modeling, and broader analyses of research evolution in mathematical geosciences. Kirkwood et al (2022); Ohmer et al (2025); Lino Pereira et al (2024); Li et al (2025); Stordal et al (2021) Additional Mathematical Geosciences applications include geostatistical uncertainty characterization for pore pressure and dual random fields for mineral potential mapping. Soares et al (2024); Riquelme (2025)

Our study integrates WOD observational coverage with these methodological themes by extracting a focused subsurface temperature field and using empirical variograms as the first step toward a nonstationary kriging framework in a well-studied ocean basin.

Foundational nonstationary spatial statistics contributions include spatial deformation, process convolution, and smooth spatially varying covariance classes, which motivate the modeling roadmap in this study. Sampson and Guttorp (1992); Higdon (1999); Paciorek and Schervish (2006)

3 Data

We use the World Ocean Database 2023 (WOD23) annual OSD (Ocean Station Data) NetCDF files hosted on the public NOAA S3 bucket. Mishonov et al (2024); Garcia et al (2024); WOD Team (2025); NOAA Open Data Dissemination Program (2026) The analysis focuses on 2010–2019 profiles in the North Atlantic (0°–60°N, 80°W–0°), selected to provide dense coverage of the Gulf Stream region and mid-latitude North Atlantic.

3.1 Provenance and extraction

Data are downloaded via the repository WOD client (`src/wod_client.py`). The specific files are: `2010/wod_osd_2010.nc` through `2019/wod_osd_2019.nc`. The retrieval date and commands are documented in `agent_run/REPRO.md`. Following NCEI guidance for temperature analyses, we also cite the World Ocean Atlas 2023 temperature volume. NOAA National Centers for Environmental Information (2025); Locarnini et al (2024)

We parse each annual file and extract temperature observations closest to 50 m depth (tolerance ±5 m). The WOD file format stores per-cast variable length profiles; we reconstruct per-cast depth and temperature arrays using the `z_row_size` and `Temperature_row_size` metadata. We retain casts where these row sizes match and where a 50 m measurement is available within the tolerance window. We filter observations using WOD quality-control flags, retaining only accepted profile and value flags (Temperature_WODprofileflag = 0, Temperature_WODflag = 0) and accepted depth flags (z_WODflag = 0) when available in the NetCDF files.

3.2 Working dataset

The resulting dataset contains 2,618 observations with latitude, longitude, timestamp, depth, and temperature. Longitude is normalized to $[-180°, 180°]$ for spatial calculations. This table serves as the input for variogram analysis and subsequent geostatistical modeling.

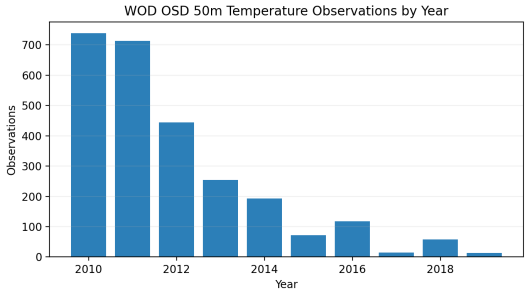

Fig. 1 Number of 50 m temperature observations by year in the working dataset.

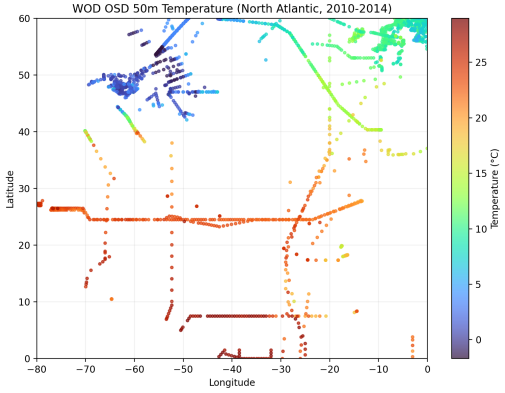

Fig. 2 Locations and temperatures of 50 m observations in the North Atlantic, 2010–2019.

4 Methods

Let $T(s,t)$ denote temperature at location s (latitude/longitude) and time t (date). We decompose observations into a large-scale trend and a spatially correlated residual:

$$T(s,t) = m(s,t) + \epsilon(s),$$

where $m(s,t)$ is a deterministic trend (linear in latitude/longitude with seasonal harmonic terms in month) and $\epsilon(s)$ is a zero-mean spatial process. We estimate $m(s,t)$ by least squares and compute residuals $r_i = T(s_i,t_i) - \hat{m}(s_i,t_i)$ for variogram analysis.

4.1 Empirical variogram

For residuals r_i at locations s_i, the empirical semivariogram is

$$\hat{\gamma}(h) = \frac{1}{2|N(h)|} \sum_{(i,j)\in N(h)} (r_i - r_j)^2,$$

where $N(h)$ is the set of pairs whose separation distances fall in a bin around lag h. Distances are computed via the haversine formula on the sphere. We bin distances up to 2,000 km and inspect isotropic and directional structure. Cressie (1993); Chilès and Delfiner (2012); Journel and Huijbregts (1978)

4.2 Parametric variogram models

We fit three common stationary variogram models with nugget: exponential, spherical, and Gaussian. For lag h and parameters (τ^2, σ^2, a) (nugget, partial sill, range), the models are

$$\gamma_{\exp}(h) = \tau^2 + \sigma^2 \left(1 - e^{-h/a}\right), \quad \gamma_{\mathrm{sph}}(h) = \tau^2 + \sigma^2 \left(1.5\frac{h}{a} - 0.5\left(\frac{h}{a}\right)^3\right),$$

for $h \le a$ and $\gamma_{\mathrm{sph}}(h) = \tau^2 + \sigma^2$ for $h > a$, and

$$\gamma_{\mathrm{gau}}(h) = \tau^2 + \sigma^2 \left(1 - e^{-(h/a)^2}\right).$$

We estimate parameters by weighted least squares on empirical semivariances, using bin counts as weights. Uncertainty is summarized via bootstrap resampling of the observation set, refitting the variogram models for each resample.

4.3 Cross-validation

We evaluate predictive performance by K-fold cross-validation on a spatial block design to reduce leakage from nearby observations. The study region is partitioned into square blocks in kilometer coordinates and folds are assigned at the block level. We compare (i) a trend-only model in latitude, longitude, month, and seasonal harmonics, and (ii) a trend-plus-Gaussian-process residual model with stationary kernels. Spatial coordinates are converted to approximate kilometer units via an equirectangular projection using the mean latitude. We report RMSE, MAE, and mean negative log-likelihood (NLL) on held-out data.

4.4 Local nonstationary approximation

To probe nonstationarity without a full spatially varying kernel, we employ a local Gaussian process approximation. For each prediction location, we select the k nearest training points in kilometer coordinates and fit a stationary Matérn GP to the residuals on this local subset, yielding spatially varying effective length scales. This provides a pragmatic nonstationary baseline for comparison against global stationary models.

4.5 Nonstationary kriging roadmap

To capture spatially varying correlation lengths, we target nonstationary covariance models that allow local adaptation in anisotropy and range. Classic approaches include spatial deformation (Sampson and Guttorp, 1992) and process-convolution constructions (Higdon, 1999), while kernel-based formulations such as the Paciorek–Schervish class provide smooth spatially varying covariance parameters. (Paciorek and Schervish, 2006) Recent Mathematical Geosciences work revisits nonstationary and anisotropic kriging in applied settings. (Grimaud et al, 2025; Gomes Gonçalves and Wellmann, 2025)

We consider a locally adaptive kernel $C(s, s')$ whose parameters vary with space, and compare against stationary exponential and Matérn baselines. Kriging predictions and uncertainty will be computed on a regular grid within the study domain, with model selection guided by cross-validation and variogram fit diagnostics. Dowd and Pardo-Igúzquiza (2024); Rasmussen and Williams (2006); Stein (1999); Cressie and Wikle (2011)

5 Experiments

We conduct exploratory spatial diagnostics as a first step toward kriging-based mapping. The workflow consists of:

1. Extract 50 m temperature observations from annual WOD OSD files (2010–2019) within the North Atlantic domain, retaining only accepted WOD quality-control flags for profile, temperature, and depth.
2. Detrend observations with a linear model in latitude/longitude and seasonal harmonics of month.
3. Compute empirical isotropic and directional variograms on residuals, using spherical haversine distances and binning up to 2,000 km.
4. Fit parametric variogram models (exponential, spherical, Gaussian) by weighted least squares and compare residual sums of squares.
5. Evaluate predictive performance with spatial block K-fold cross-validation, comparing a linear trend baseline to Gaussian process residual models (RBF and Matérn kernels) using equirectangular kilometer coordinates, and to a local-GP nonstationary approximation based on nearest neighbors.

We use a random subsample of 500 observations per variogram for computational tractability and report semivariance as a function of distance. For variogram parameter uncertainty, we run 40 bootstrap resamples. Directional variograms focus on north–south (0°) and east–west (90°) axes with a 22.5° angular tolerance. These diagnostics guide subsequent selection of stationary or nonstationary covariance models.

As a baseline interpolation, we fit a stationary Gaussian process regression model with an isotropic RBF kernel (equivalent to ordinary kriging under a Gaussian covariance). Latitude/longitude are converted to equirectangular kilometer coordinates before fitting. Predictions are produced on a 1° grid over the study region to visualize large-scale structure.

6 Results

The working dataset contains 2,618 50 m temperature observations from 2010–2019, with coverage concentrated in the western and central North Atlantic (Figure 2). Temperatures range from −1.71°C to 28.98°C with a mean of 10.35°C, reflecting a mix of subtropical and subpolar conditions at 50 m depth. Sampling is uneven over time, with most observations from 2010–2012 and sparse coverage after 2016.

The empirical isotropic variogram (Figure 4) suggests spatial dependence at basin scales, motivating a range parameter on the order of 1,000–1,500 km for baseline models. Directional variograms indicate modest anisotropy for east–west versus north–south separations (Figure 4), consistent with oceanographic structure in the Gulf Stream and subpolar gyre.

Parametric fits to the empirical variogram (Figure 4) yield nugget, sill, and range estimates of roughly (τ^2, σ^2, a) equal to (3.68, 11.75, 881 km) for the Gaussian model, (2.10, 19.93, 1,570 km) for the exponential, and (2.01, 12.99, 1,729 km) for the spherical. The Gaussian model provides the lowest weighted residual sum of squares among these three fits, though all capture basin-scale dependence. A 40-resample bootstrap yields a 95% interval for the Gaussian range of roughly 671–1,058 km, indicating moderate uncertainty in length-scale estimates.

Cross-validation indicates that augmenting the linear trend with a stationary Gaussian process improves predictive skill under spatial blocking. On a 4-fold spatial-block split (400 km blocks) of a 400-point subsample, the trend-only baseline attains RMSE 4.43°C and MAE 3.72°C, while the trend+GP models achieve RMSE 2.48–2.54°C and MAE 1.98–2.03°C. The Matérn kernel yields the best mean NLL among these stationary baselines. A local-GP nonstationary approximation with $k = 80$ nearest neighbors is weaker (RMSE 2.65°C, MAE 2.13°C), suggesting that further nonstationary structure must be modeled more explicitly. Fold-to-fold variability is nontrivial under spatial blocking (Table 1). A block-size check indicates that qualitative rankings are stable for 300–500 km blocks, with RMSE shifts of a few tenths of a degree (Table 2).

Table 1 Spatial-block cross-validation metrics (4 folds, 400 km blocks, 400-point subsample). Values are mean ± SD across folds.

Model	RMSE (°C)	MAE (°C)	Mean NLL
Trend only	4.43 ± 0.69	3.72 ± 0.71	3.16 ± 0.03
Trend + GP (Matérn)	2.47 ± 0.64	1.98 ± 0.52	2.44 ± 0.46
Trend + GP (RBF)	2.54 ± 0.62	2.03 ± 0.51	2.47 ± 0.44
Trend + local GP (Matérn, $k = 80$)	2.65 ± 0.37	2.13 ± 0.44	2.55 ± 0.07

Table 2 Sensitivity of spatial-block cross-validation to block size (400-point subsample). Values are mean RMSE ± SD across folds.

Model	300 km blocks	400 km blocks	500 km blocks
Trend only	4.27 ± 0.44	4.43 ± 0.69	4.46 ± 0.46
Trend + GP (Matérn)	2.18 ± 0.46	2.47 ± 0.64	2.35 ± 0.90
Trend + GP (RBF)	2.25 ± 0.47	2.54 ± 0.62	2.49 ± 0.89
Trend + local GP (Matérn, $k = 80$)	2.22 ± 0.55	2.65 ± 0.37	2.42 ± 0.51

The stationary Gaussian process baseline (Figure 3), fit on equirectangular kilometer coordinates, captures the broad meridional gradient between subtropical and subpolar waters but smooths over mesoscale structure. This motivates future nonstationary covariance models.

7 Discussion

The empirical variograms indicate spatial correlation of 50 m temperature residuals at basin scales, suggesting that simple stationary covariance models may capture first-order structure but miss regional nonstationarity associated with western boundary currents and subpolar fronts. Directional differences between north–south and east–west semivariance are consistent with anisotropic processes in the North Atlantic.

Limitations include uneven temporal sampling (fewer casts in later years), as shown by the observation map and year-count figure. Additional concerns are instrument heterogeneity and simplified detrending; although seasonal harmonics reduce annual cycle bias, residual mesoscale and interannual variability remain. Spatial block cross-validation mitigates leakage but lowers effective sample size, motivating larger data volumes or spatiotemporal models. Future work will explore richer trend models, explicit spatiotemporal covariance, and nonstationary kernels informed by bathymetry and ocean circulation features.

8 Conclusion

We assembled a reproducible WOD23-based dataset of 50 m temperature in the North Atlantic (2010–2019), and used empirical variograms to characterize spatial dependence and anisotropy. Stationary Gaussian process baselines outperform a trend-only model in spatial-block cross-validation, while a local-GP

nonstationary approximation does not improve predictive skill on the current subsample. These results provide quantitative baselines and motivate future work on richer spatiotemporal and physics-informed nonstationary covariance models. The pipeline and analysis scripts provide a basis for expanding to additional depths, variables, and validation designs.

Acknowledgments

Add acknowledgments and funding sources, if any.

References

Abulkhair S, Dowd PA, Xu C (2023) Geostatistics in the presence of multivariate complexities: Comparison of multi-gaussian transforms. Mathematical Geosciences 55:713–734, DOI 10.1007/s11004-023-10056-y, URL https://link.springer.com/article/10.1007/s11004-023-10056-y, published 05 April 2023

Boyer TP, Levitus S (2006) World ocean database 2005. Tech. Rep. 60, National Oceanographic Data Center, URL https://repository.library.noaa.gov/view/noaa/1131

Boyer TP, Antonov JI, Baranova OK, et al (2009) World ocean database 2009. Tech. Rep. 66, National Oceanographic Data Center, URL https://repository.library.noaa.gov/view/noaa/1195

Boyer TP, Antonov JI, Baranova OK, et al (2013) World ocean database 2013. Tech. Rep. 72, National Oceanographic Data Center, DOI 10.7289/V5NZ85MT, URL https://repository.library.noaa.gov/view/noaa/1291

Boyer TP, Garcia HE, Locarnini RA, Zweng MM, Mishonov AV, Reagan JR, Weathers KA, Baranova OK, Paver CR, Seidov D, Smolyar I (2018) World ocean database 2018. Tech. Rep. 87, NOAA National Centers for Environmental Information

Chilès JP, Delfiner P (2012) Geostatistics: Modeling Spatial Uncertainty. John Wiley & Sons

Cressie N, Wikle CK (2011) Statistics for Spatio-Temporal Data. John Wiley & Sons, Hoboken, NJ, URL https://academic.oup.com/biometrics/article-abstract/68/4/1328/7394105

Cressie NAC (1993) Statistics for Spatial Data. John Wiley & Sons, New York, URL https://emu.tind.io/record/172938

De Iaco S, Hristopulos DT, Lin G (2022) Special issue: Geostatistics and ml. Mathematical Geosciences 54:459–465, DOI 10.1007/s11004-022-09998-6, URL https://link.springer.com/article/10.1007/s11004-022-09998-6

Dowd PA, Pardo-Igúzquiza E (2024) The many forms of co-kriging: A diversity of multivariate spatial estimators. Mathematical Geosciences 56:387–413, DOI 10.1007/s11004-023-10104-7, URL https://link.springer.com/article/10.1007/s11004-023-10104-7

Garcia HE, Boyer TP, Locarnini RA, Reagan JR, Mishonov AV, Baranova OK, Paver CR, Wang Z, Bouchard CN, Cross S, Seidov D, Dukhovskoy D (2024) World ocean database 2023 user's manual. Tech. Rep. 98, NOAA National Environmental Satellite, Data, and Information Service; NOAA National Centers for Environmental Information, DOI 10.25923/j8gq-ee82, URL https://repository.library.noaa.gov/view/noaa/66124

Gomes Gonçalves Í, Wellmann F (2025) Uncertainty propagation in deep gaussian process networks. Mathematical Geosciences 57:1115–1133, DOI 10.1007/s11004-025-10187-4, URL https://link.springer.com/article/10.1007/s11004-025-10187-4

Grimaud JL, Desassis N, Chourio-Camacho D, Renard D, Pereira M, Ors F, Tissoux H, Bessin P, Noble M, et al (2025) Kriging alluvial thicknesses in valley bottoms using nonstationary geometric anisotropies. Mathematical Geosciences 57:1379–1399, DOI 10.1007/s11004-025-10200-w, URL https://link.springer.com/article/10.1007/s11004-025-10200-w

Higdon D (1999) Non-stationary spatial modeling. In: Bayesian Statistics 6: Proceedings of the Sixth Valencia International Meeting, Oxford University Press, pp 761–768, DOI 10.1093/oso/9780198504856.003.0036, URL https://academic.oup.com/book/53983/chapter/422202601

Journel AG, Huijbregts CJ (1978) Mining Geostatistics. Academic Press, London; New York, URL https://catalogue.nla.gov.au/Record/1116468

Kirkwood C, Economou T, Pugeault N, Odbert H (2022) Bayesian deep learning for spatial interpolation in the presence of auxiliary information. Mathematical Geosciences 54:507–531, DOI 10.1007/s11004-021-09988-0, URL https://link.springer.com/article/10.1007/s11004-021-09988-0

Li W, Wang Z, Ma X (2025) Mapping the evolution of mathematical geoscience research with big literature data and context-aware text mining. Mathematical Geosciences 57:799–820, DOI 10.1007/s11004-025-10179-4, URL https://link.springer.com/article/10.1007/s11004-025-10179-4, published 05 March 2025

Lino Pereira J, Varouchakis EA, Karatzas GP, Azevedo L, et al (2024) Uncertainty quantification in geostatistical modelling of saltwater intrusion at a coastal aquifer system. Mathematical Geosciences 56:867–885, DOI 10.1007/s11004-023-10120-7, URL https://link.springer.com/article/10.1007/s11004-023-10120-7, published 02 January 2024

Locarnini RA, Mishonov AV, Baranova OK, Reagan JR, Boyer TP, Seidov D, Wang Z, Garcia HE, Bouchard C, Cross SL, Paver CR, Dukhovskoy D (2024) World ocean atlas 2023, volume 1: Temperature. Tech. Rep. 89, NOAA National Centers for Environmental Information, DOI 10.25923/54bh-1613, URL https://repository.library.noaa.gov/view/noaa/60599, a. Mishonov, Technical Ed.; 40 pp.

Miao C, Wang Y (2025) Sparse spectrum representation of gaussian process regression for modeling nonstationary geo-data from limited measurements. Mathematical Geosciences DOI 10.1007/s11004-025-10243-z, URL https://link.springer.com/article/10.1007/s11004-025-10243-z, published 02 December 2025

Mishonov AV, Boyer TP, Baranova OK, Bouchard CN, Cross S, Garcia HE, Locarnini RA, Paver CR, Reagan JR, Wang Z, Seidov D, Grodsky AI, Beauchamp JG (2024) World ocean database 2023. Tech. Rep. 97, NOAA National Environmental Satellite, Data, and Information Service; NOAA National Centers for Environmental Information, DOI 10.25923/z885-h264, URL https://repository.library.noaa.gov/view/noaa/66204, c. Bouchard, Technical Ed.; 206 pp.

NOAA National Centers for Environmental Information (2025) World ocean database data product series metadata. Accessed 2026-01-02

NOAA National Centers for Environmental Information (2026) World ocean database. Accessed 2026-01-02

NOAA Open Data Dissemination Program (2026) Noaa world ocean database (wod) - registry of open data on aws. URL https://registry.opendata.aws/noaa-wod/, accessed 2026-01-02

Ohmer M, Doll F, Liesch T (2025) Incorporating spatial information for regionalization of environmental parameters in machine learning models. Mathematical Geosciences 57:251–273, DOI 10.1007/s11004-024-10163-4, URL https://link.springer.com/article/10.1007/s11004-024-10163-4, published 18 December 2024

Paciorek CJ, Schervish MJ (2006) Spatial modelling using a new class of nonstationary covariance functions. Environmetrics 17(5):483–506, DOI 10.1002/env.785, URL https://pmc.ncbi.nlm.nih.gov/articles/PMC2157553/

Rasmussen CE, Williams CKI (2006) Gaussian Processes for Machine Learning. MIT Press, Cambridge, MA, URL https://is.mpg.de/publications/3569

Riquelme AI (2025) Dual random fields and their application to mineral potential mapping. Mathematical Geosciences 57:845–881, DOI 10.1007/s11004-025-10195-4, URL https://link.springer.com/article/10.1007/s11004-025-10195-4, published 17 June 2025

Sampson PD, Guttorp P (1992) Nonparametric estimation of nonstationary spatial covariance structure. Journal of the American Statistical Association 87(417):108–119, DOI 10.1080/01621459.1992.10475181, URL https://www.jstor.org/stable/2290458

Soares A, Nunes R, Salvadoretti P, Costa JF, Martins T, Santos M, Azevedo L, et al (2024) Pore pressure uncertainty characterization coupling machine learning and geostatistical modelling. Mathematical Geosciences 56:691–709, DOI 10.1007/s11004-023-10102-9, URL https://link.springer.com/article/10.1007/s11004-023-10102-9, published 06 November 2023

Stein ML (1999) Interpolation of Spatial Data: Some Theory for Kriging. Springer Series in Statistics, Springer, DOI 10.1007/978-1-4612-1494-6, URL https://link.springer.com/book/10.1007/978-1-4612-1494-6

Stordal AS, Moraes RJ, Raanes PN, Evensen G (2021) p-kernel stein variational gradient descent for data assimilation and history matching. Mathematical Geosciences 53:375–393, DOI 10.1007/s11004-021-09937-x, URL https://link.springer.com/article/10.1007/s11004-021-09937-x, published 17 March 2021

Talebi H, Peeters LJM, Mueller U, Tolosana-Delgado R, van den Boogaart KG (2020) Towards geostatistical learning for the geosciences: A case study in improving the spatial awareness of spectral clustering. Mathematical Geosciences 52:1035–1048, DOI 10.1007/s11004-020-09867-0, URL https://link.springer.com/article/10.1007/s11004-020-09867-0, published 08 June 2020

WOD Team (2025) World ocean database data product series. Dataset, NOAA National Centers for Environmental Information, DOI 10.25921/v92s-y066, URL https://doi.org/10.25921/v92s-y066, accessed 2026-01-02

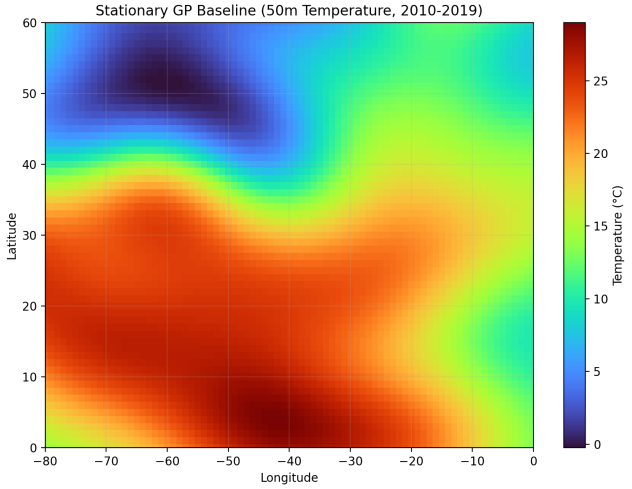

Fig. 3 Stationary Gaussian process baseline (1° grid), fit in equirectangular kilometer coordinates.

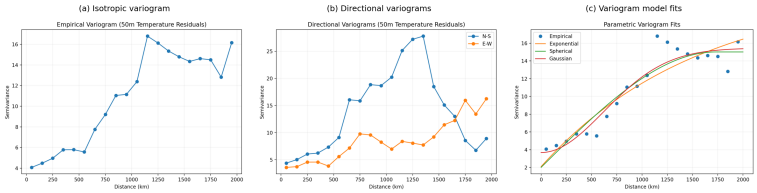

Fig. 4 Variogram diagnostics: (a) isotropic variogram of detrended 50 m temperature residuals, (b) directional variograms, and (c) parametric model fits.